Journal of The Electrochemical Society, **157** (11) B1624-B1628 (2010)
0013-4651/2010/157(11)/B1624/5/$28.00 © The Electrochemical Society

Effect of $La_2Zr_2O_7$ on Interfacial Resistance in Solid Oxide Fuel Cells

A. Chen,[a] J. R. Smith,[a] K. L. Duncan,[a] R. T. DeHoff,[b] K. S. Jones,[b,*] and E. D. Wachsman[c,,z]**

[a]*Florida Institute for Sustainable Energy and* [b]*Department of Materials Science and Engineering, University of Florida, Gainesville, Florida 32611-6400, USA*
[c]*University of Maryland Energy Research Center, University of Maryland, College Park, Maryland 20742, USA*

The impact of $La_2Zr_2O_7$ (LZO) on interfacial resistance (R_p) at the $La_{0.78}Sr_{0.20}MnO_{3-\delta}$/yttria-stabilized zirconia interface was studied upon isothermal sintering at 1200°C for 2–25 h. Quantification of triple phase boundary length was performed by applying focused ion beam/scanning electron microscopy (FIB/SEM) serial-sectioning techniques and classical stereology. Electrochemical impedance spectroscopy was used to characterize the R_p. The effect of LZO formation on microstructural models for R_p was analyzed with respect to previous works that did not include this effect. LZO formation modifies the TPB length, rapidly increases R_p, and needs to be controlled in analytical microstructural R_p models.
 [DOI: 10.1149/1.3484092]

Manuscript submitted June 7, 2010; revised manuscript received August 9, 2010. Published September 14, 2010.

Solid oxide fuel cells (SOFC) are energy conversion devices with great promise because they are environmentally friendly, fuel flexible, and efficient. Much of these attributes arise from their high operating temperature ~600 to 1000°C.[1,2] However, high operating temperatures also result in slow startup times and performance degradation due to (*i*) insulating phases formed by chemical reactions between SOFC components[3,4] and (*ii*) microstructural instability, including coarsening.[5] For these problems to be overcome, it is crucial that their origin and the underlying mechanisms are better understood.

SOFCs produce electricity by converting the chemical energy of fuel via the following two chemical reactions: oxygen reduction (occurring at the air/cathode/electrolyte interface) and hydrogen/fuel oxidation (occurring at the fuel/anode/electrolyte interface). Conversion efficiency and power density are collectively determined by three types of cell polarizations: (*i*) ohmic polarization, (*ii*) concentration polarization, and (*iii*) activation polarization. Ohmic polarization is reduced by using highly conductive and/or thin-film electrolytes, while concentration polarization, related to gas phase transport in porous media, is controlled by optimizing electrode microstructures.

Activation polarization is determined by the kinetics of the chemical reactions, with the oxygen reduction reaction (ORR) currently being the more limiting of the two.[5-7] Moreover, at low to moderate loads, activation polarization is the dominant factor in reduced efficiency in state-of-the-art SOFCs. Accordingly, this paper seeks to address the impact of processing and geometric variables on the performance of SOFC cathodes with the intent of identifying underlying causes of activation polarization in conventional SOFCs containing lanthanum-based perovskite cathodes and yttria-stabilized zirconia (YSZ) electrolytes.

The ORR is written, in Kröger–Vink notation,[8] as follows

$$\frac{1}{2}O_2(g) + 2e' + V_O^{\bullet\bullet} \rightarrow O_O^{\times} \quad [1]$$

Equation 1 shows that, to produce lattice oxygen ($O_O^{\times}$), the ORR combines three different species: ions (i.e., oxygen vacancies, $V_O^{\bullet\bullet}$), electrons (e'), and gas molecules. However, assembling these species at a suitable location, i.e., a triple phase boundary (TPB) (where gas, electrolyte, and cathode coincide), requires several steps including but not limited to the following:[8]

1. Oxygen gas transport through pores within the cathode.
2. Surface adsorption of oxygen molecules on the porous electrode.
3. Dissociation of adsorbed oxygen molecules (O_{ads}) on the porous electrode or dense electrolyte.
4. Surface diffusion of adsorbed oxygen atom to the TPB.
5. Charge transfer among O_{ads}, e^-, and vacancy at the TPB.

Hence, several variables can, and do, affect the ORR processes occurring at the cathode. Therefore, all ORR processes are influenced by the geometric parameters of the cathode microstructure.

The kinetics of the (major) ORR steps may be modeled by their effective resistances.[9] This is called the three-link paradigm among microstructural properties, chemical reaction mechanisms, and cathode polarization. Many studies in this area employed electrical impedance spectroscopy (EIS) to examine the influence of one-dimensional and two-dimensional (2D) metrics of cathode microstructures on the chemical reaction rate and interfacial resistances.[10-15] Indeed, some were able to deconvolute impedance spectra to assign a specific resistance for each ORR step.[16] For example, a frequently investigated metric is TPB length, L_{TPB}, unit length per area ($\mu m/\mu m^2$), which is a key factor governing the efficiency of the charge-transfer reaction occurring at the electrode/electrolyte interface.[10,13-15,17,18]

Mizusaki et al.[10] assumed that the dissociation of adsorbed oxygen gas occurs at the YSZ/pore interface, followed by the surface diffusion of dissociated oxygen atoms along the YSZ/pore interface to the TPB. Their investigations concluded that the interfacial resistance, R_p is dominated by oxygen incorporation into the electrolyte and is controlled by the reaction rate at the TPB.

In their study, a depressed arc in the Nyquist plot was interpreted using a simple resistor–capacitor equivalent circuit model, and R_p was determined to be inversely proportional to the exchange current density. Because the exchange current density is roughly proportional to L_{TPB}, they argue that, $R_P \sim 1/L_{TPB}$.[19] L_{TPB} in this particular study was not experimentally measured. Instead, it was deduced from a simple, geometrically idealized model using circles to represent the grains of the porous cathode microstructure.

In a second study, Kuznecov et al.[14] etched away the cathode to determine L_{TPB} at the $La_{0.8}Sr_{0.2}MnO_3$ (LSM)/YSZ interface. This technique has a potentially serious weakness, however, as it is likely that the geometrical parameters of the TPB were affected by the etchant.[14] Moreover, though LSM is generally considered to be an electronically conducting cathode with a negligible oxygen solid-state transport, Kuznecov et al. assumed LSM as a mixed electronic and ionic conducting cathode and, therefore, that the oxygen transport at the $La_{0.8}Sr_{0.2}MnO_3$/YSZ interface is controlled by bulk dif-

* Electrochemical Society Active Member.
** Electrochemical Society Fellow.
z E-mail: ewach@umd.edu

fusion of oxygen vacancies.[14] With these assumptions, Kuznecov et al. applied a bulk-diffusion controlled oxygen reduction model[17] and concluded that R_p is a function of contact area between the cathode and the electrolyte, S_c, as well as TPB length. In addition, because Adler et al. asserted that R_p depends not only on the microstructure (L_{TPB}, S_c, and porosity) but also on the electrocatalytical properties of the cathode material,[17] Kuznecov et al. then deduced, for a bulk-diffusion controlled model, that $R_p \sim (L_{TPB}S_c)^{-0.5}$.[14]

The ORR model and the experimental and modeling techniques used to obtain L_{TPB} are key factors in the accurate determination of the dependence of R_p on geometric parameters of the cathode microstructure. Clearly, R_p depends on the diffusion paths for oxygen through the cathode materials.[10,20-22] In addition, the quantification of L_{TPB} depends on the geometric model used to extract L_{TPB} from the microstructure. Finally, LSM reacts with YSZ to form a deleterious tertiary phase at the LSM/YSZ interface at normal operating temperatures ~700 to 1000°C.[3] It is therefore important to study the influence of the tertiary phase on the relationship between the R_p and the L_{TPB}. This final but crucial refinement is absent from previous studies,[10,14,19] including the ones described above.

In this paper, focused ion beam/scanning electron microscopy (FIB/SEM) was employed to expose TPB at the LSM/YSZ interface, thereby avoiding the introduction of etching artifacts into the quantification of L_{TPB}. Cross-serial sectioning techniques using FIB/SEM and a classical stereological model was used to quantify the representative L_{TPB} and S_c. R_p, measured by EIS, were correlated with L_{TPB} and S_c. These data were compared with the two previous microstructural R_p models described above, and a new microstructural R_p model was developed that includes the effects of the formation of deleterious secondary phases. This study provides a new perspective on the influence of the growth of secondary phases on the degradation of SOFC electrochemical properties.

Experimental

Samples of 180 μm thick, 10 × 20 mm YSZ (8 mol %) electrolyte were obtained from Marketech International. $La_{0.78}Sr_{0.20}MnO_{3-\delta}$ ink provided by Nextech Materials was screen-printed on both sides of the electrolyte giving a cathode area of 64 mm^2 each. A drying step was performed in a Fisher Isotemp drying oven at 120°C for 2 h. After drying, eight samples were sintered at 1200°C at times ranging from 2 to 25 h in a Lindberg/Blue high temperature box furnace. The resulting cathode thickness is about 43 μm.

The slight A-site deficiency (2 %) of the $La_{0.78}Sr_{0.20}MnO_{3-\delta}$ (LSM^*) ink used in this study is noted here. A-site deficient LSM is typically used in SOFCs specifically because it is less reactive with YSZ than stoichiometric LSM. Consequently, the formation of secondary phases would be expected to increase with stoichiometric LSM under identical experimental conditions. However, the intent here was to determine the effects on interfacial resistance with conventionally used compositions.

The FIB/SEM experimental design was performed to enable unbiased quantification of 2D and three-dimensional geometric properties of the cathode.[23] The FIB/SEM was operated at an electron-beam energy of 5 kV and a Ga^+ ion beam current of 300 pA. Thirty stacks of five cross-serial sections with a spacing of approximately one-fifth of the pore size were taken first from an area on the cathode of 15 × 20 μm. The magnification of the cross section image was 15,000×. Open pores at the LSM^*/YSZ interface were identified by observing pore evolutions in sequential slices. The homogeneity of the distribution of the pore network for the isothermally sintered samples was examined using dissector analysis of the connectivity density.[23] A volume of 15 × 15 × 20 μm was investigated. Connectivity density analysis coupled with a t-test (i.e., using the statistical student's t-distribution) was performed to determine the optimum number of cross-section images.[23] Then 25 cross-section images with the spacing of the pore size were taken randomly from this set of 150 cross-section images. Quantification of L_{TPB} and S_c was representative by applying the classical stereology models. A line probe was applied across the LSM^*/YSZ interface to quantify L_{TPB} by calculating the number of interceptions per unit length, and two line probes were placed on the 25 cross section with random angles to quantify surface area, porosity,[23] and S_c.

Transmission electron microscopy (TEM) cross-section foils of seven samples were prepared with a Dual Beam FIB system and an in situ Omniprobe manipulator at the LSM^*/YSZ interface. Structural analysis of the LSM^*/YSZ interface was performed by high resolution TEM. Scanning transmission electron microscopy–energy-dispersive X-ray spectrometry was used for chemical characterization of the LSM^*/YSZ interface. The tertiary phase thickness was measured based on bright-field images taken by the high resolution TEM. Further details of the experimental procedure are described by Chen et al.[4]

EIS using a Solartron 1260 impedance gain analyzer was performed to measure the frequency response of the prepared samples in air at 900°C. A 50 mV ac voltage was applied and the induced current was measured to produce the impedance spectra. Measurement was made via a two-point connection to the Solartron. Auto-integration was used under "I, long" measurement conditions with an integration time of 60 s. "I, long" is a Zplot option in which the current is measured for noise and an attempt is made to get consistency in the measurements with a maximum standard deviation of 1% when possible. The active frequency range was 1.0×10^{-2}–3.2×10^7 Hz. SMART, Zplot, and Zview were used to acquire and display the impedance data. High frequency and low frequency intercepts in Nyquist plots were recorded. Interfacial resistance was obtained by calculating the mathematical difference between the two intercepts with the real impedance axis[24,25] and dividing by 2 (because symmetric cells were used).

Results and Discussion

The effect of sintering on the cathode microstructure.— Figure 1a shows the TPB length as a function of the sintering time. The area normalized TPB length initially increased to a maximum (0.9 $\mu m/\mu m^2$) and then decreased to 0.4 $\mu m/\mu m^2$ as the sintering time increased. This is consistent with changes in TPB length observed in samples sintered at 1100°C from 10 min to 10^3 min based on atomic force microscopy measurement.[26] Figure 1b shows the contact area as a function of sintering time. The contact area between the LSM^* and YSZ increases as the sintering time increases. Figure 1c shows that $La_2Zr_2O_7$ (LZO) thickness increases as the sintering time increases. The small error bars of the LZO thickness come from six repeatable measurements for each sample.

Variation in the TPB length is attributed to changes in effective contact area between the LSM^* grains and the YSZ. Early in the sintering process (less than 8 h), contacts among LSM^* grains and between LSM^* and YSZ increase and point-to-point contacts change into face-to-face contacts, increasing TPB length. Likewise, increasing contact area arises from the increase in the face-to-face contact between the LSM^* and the YSZ. LSM^* grain growth tends to increase contact area as the sintering time increases up to 8 h, whereas, after sintering for 8 h, formation of closed pore channels decreases the effective contact area between the LSM^* grains and the YSZ. As a result, TPB length dramatically reduces though contact area continues to increase.

The linear relationship between the LZO thickness and the logarithm of sintering time might indicate the parabolic growth of the LZO layer.[4] The impact of the LZO thickness on TPB length and contact area is addressed in a later section.

Contributions of the metric properties to the interfacial resistance.— Figure 2a shows a Nyquist plot of the isothermally sintered samples. The real component of the impedance, i.e., the interfacial resistance, increases with sintering time. Interfacial resistance as a function of the sintering time is shown in Fig. 2b. The interfacial resistance increases from 120 to 300 Ω cm^2 as the sintering time increases from 2 to 25 h.

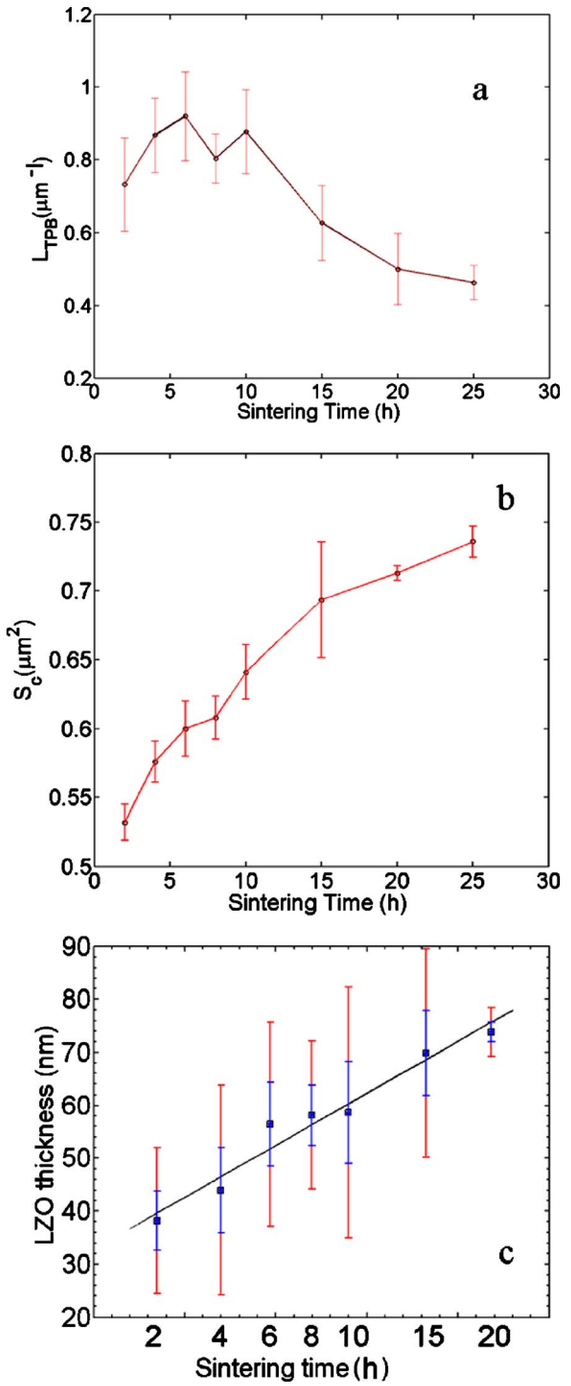

Figure 1. (Color online) Metric properties as a function of the sintering time: (a) TPB length, (b) contact area, and (c) LZO thickness.

The comparison of the interfacial resistance to the TPB and contact area is shown in Fig. 3. The close fit between data in this paper and Mizusaki's model (model 1) should be noted. Figure 3a shows that as L_{TPB} decreases, the interfacial resistance, R_p increases, following the trend ($R_p \sim L_{TPB}^{-1}$). In Mizusaki's model impedance circuit, Warburg impedance and diffusion of oxygen in pores were taken into account.

Figure 3b shows comparison of the interfacial resistance to the bulk diffusion volume (the product of the L_{TPB} and S_c) as obtained by Kuznecov et al. (model 2). Large differences can be observed

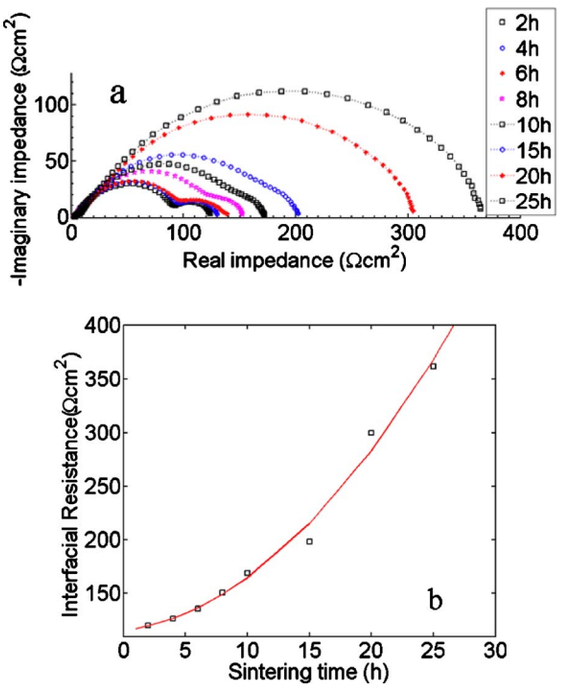

Figure 2. (Color online) Impedance profile of the isothermal sintering samples: (a) Nyquist plot and (b) time dependence of the interfacial resistance.

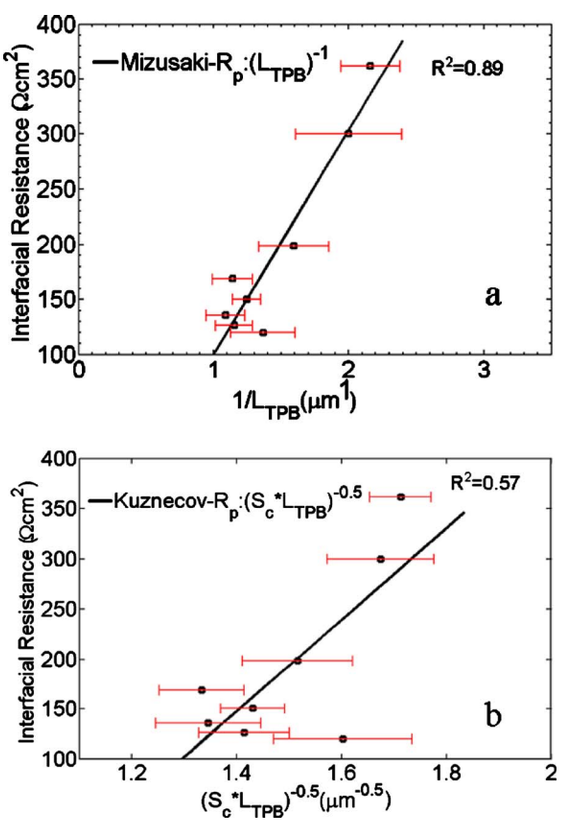

Figure 3. (Color online) Comparison between this work and the two models; note that the *R*-squared values are higher in (a) than in (b).

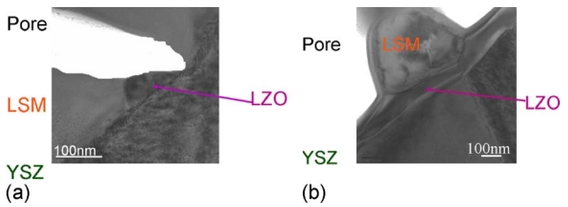

Figure 4. (Color online) The effect of LZO growth at early stage (a) and after longer term sintering (b).

between our data and Kuznecov's model. The data trend did not follow a −0.5 power dependence of the interfacial resistance on the product of the L_{TPB} and S_c, i.e., R_p is not proportional to $(L_{TPB}S_c)^{-0.5}$.[14] Kuznecov's model gives an inferior fit to the raw data compared to Mizusaki's model. Deviation of the data, for the isothermally sintered samples, from Kuznecov's model might be attributed to our use of single-phase LSM* cathodes. Kuznecov's model, was developed using LSM–YSZ composites which, by virtue of the microstructure, are less affected by surface migration.[14] Because the isothermally sintered samples contained pure LSM* cathodes (which is a good electronic conductor, but a poor ionic conductor), oxygen species dissociated on the cathode surface must migrate long distances (compared to an LSM–YSZ composite cathode) to the cathode–electrolyte interface before transfer into the electrolyte. Consequently, LSM electrodes do not generally exhibit behavior consistent with bulk diffusion models.[17]

Contributions of LZO formation to the interfacial resistance.— Figure 4 shows TEM bright-field images for the representative sample. The LZO phase nucleates at the TPB site where pores, LSM*, and YSZ meet (see Fig. 4a). Apparently, LZO blocks some TPB sites; in other words, effective TPB sites are reduced by the LZO formation. Because the charge-transfer reaction depends on the number of effective TPB sites, the formation of LZO causes an increase in charge-transfer resistance. So two factors contribute to the increase in the interfacial resistance: the formation of LZO phase and the reduction in L_{TPB}. It should be pointed out that LZO is an electronic insulator compared to the LSM*.[5] At the later sintering stage (see Fig. 4b), LZO covers not only the TPB sites but also the entire LSM*/YSZ interface. In this instance, the charge-transfer reaction is not localized to the original TPB. The charge-transfer reaction must now take place at sites where LZO is present, such as the pore/LSM*/LZO and/or the pore/YSZ/LZO unions. In both cases, the rate of charge transfer is reduced by decreasing the amount of active reactants or by decreasing the ORR rate constant itself because the reaction occurs at less active sites. Therefore, the formation of the LZO phase needs to be incorporated in the modeling of the interfacial resistance.

Comparing both models, our data shows the best fit with Mizusaki's model. However, it is important to know how the formation of the secondary LZO phase also plays a factor in determining the measured R_p and hence should be incorporated in each model for a truer evaluation of the models and understanding of the performance limitations of the LSM*–YSZ system. To incorporate the effects of LZO formation, consider that as the quantity of LZO increases, the thickness (t_{LZO}) of the LZO phase increases and the concentration of reaction sites decreases (i.e., by reducing TPB length). Moreover, both factors (separately or together) increase the interfacial resistance. Therefore, $R_p \sim t_{LZO}^x/(L_{TPB}f)^y$, where x and y are indexes indicative of the extent of the dependence of R_p on t_{LZO} and $L_{TPB}f$, respectively, and $f = 1$ (model 1) or S_c (model 2). Because the dependence of R_p on LZO thickness is unknown, x and y were optimized through a MATLAB code in both models. The optimum number was achieved when the least fit square was a minimum after 1000 optimization cycles.

Figure 5 shows the incorporation of the LZO phase into both models. The effect of the LZO phase on Mizusaki's model (model 1) is shown in Fig. 5a. A very plausible linear dependence of the resistance on the LZO thickness (i.e., $x = 1$) was obtained after optimization (though $x = 1.1$ shows measurable reduction in least-square residuals, the decrease in magnitude is negligible). The interfacial resistance increases linearly with LZO thickness per L_{TPB}.

Using the same optimization procedure, Fig. 5b shows that $R_p \sim t_{LZO}^{0.6}/(L_{TPB}S_c)^{0.5}$ for Kuznecov's model (model 2). Again, treating LSM* as a mixed conducting cathode causes inferior fit in this model, as Fig. 3 showed. However, including the effect of LZO results in better fits in Fig. 5b compared to Fig. 3b.

Clearly, both models improve when the LZO thickness is included. Therefore, the formation of LZO should be accounted for whenever the interfacial resistance of LSM-based cathodes (on YSZ electrolytes) is being modeled, particularly with respect to microstructural features such as TPB length.

Conclusions

FIB/SEM and stereological analysis were used to characterize the interfacial microstructure of SOFCs. Isothermal sintering of LSM* at 1200°C suggests that the interfacial resistance increases by both microstructural evolution (coarsening) and LZO phase formation.

Moreover, the TPB length is modified due to LZO phase formation at the cathode/electrolyte interface. The LZO phase hinders the supply of oxygen intermediates and obstructs the conduction of vacancies and electrons to reaction sites at the LSM*/YSZ interface. When LZO presence is significant, a reduced amount of reactant species are available resulting in reduced reaction rates, and thus, increasing charge-transfer polarization.

Clearly, the relationship between TPB length and the interfacial resistance with LZO phase formation is different from the case without LZO phase formation. Therefore, microstructurally based cathodic polarization models should include LZO phase formation if they are to accurately portray the phenomena involved, particularly for cathodes processed at high temperature (~1200°C) or for high temperature operating conditions (~1000°C).

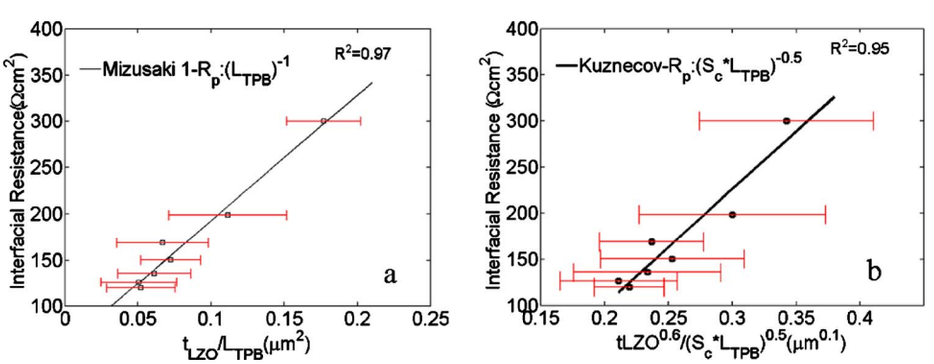

Figure 5. (Color online) Effect of LZO layer in comparison between this work and two models; note that the *R*-squared values are better than the previous figures.

Acknowledgments

The authors thank the University of Florida and the U.S. Department of Energy High Temperature Electrochemistry Center for funding the project (DE-AC05-76RL01830). We also thank the Major Analytical Instrumentation Center, Department of Materials Science and Engineering, University of Florida for the use of their facilities.

University of Maryland assisted in meeting the publication costs of this article.

References

1. E. Baur and H. Precis, *Z. Elektrochem.*, **43**, 727 (1937).
2. H. W. C. Heraeus, *Z. Elektrochem.*, **6**, 41 (1899).
3. S. K. Lau and S. C. Singhal, in *Corrosion 85*, Vol. 1–9, p. 345, The National Association of Corrosion Engineers, Houston, TX (1985).
4. A. Chen, G. Bourne, K. Siebein, R. DeHoff, E. Wachsman, and K. Jones, *J. Am. Ceram. Soc.*, **91**, 2670 (2008).
5. S. C. Singhal and K. Kendall, *High Temperature Solid Oxide Fuel Cells: Fundamentals, Design and Applications*, Elsevier, Oxford, UK (2003).
6. O. Yamamoto, Y. Takeda, R. Kanno, and T. Kojima, in *Proceedings of the International Symposium on Solid Oxide Fuel Cell*, SOFC Society of Japan, p. 87 (1989).
7. J. A. Labrincha, J. R. Frade, and F. M. B. Marques, *J. Mater. Sci.*, **28**, 3809 (1993).
8. S. C. Singhal, *MRS Bull.*, **16**, 25 (2000).
9. B. C. H. Steele, *Solid State Ionics*, **134**, 3 (2000).
10. J. Mizusaki, H. Tagawa, K. Tsuneyoshi and A. Sawata, *J. Electrochem. Soc.*, **138**, 1867 (1991).
11. A.V. Virkar, J. Chen, C. W. Tanner and J. W. Kim, *Solid State Ionics*, **131**, 189 (2000).
12. T. Kenjo, Y. Yamakoshi, and K. Wada, *J. Electrochem. Soc.*, **140**, 2151 (1993).
13. M. Kleitz, L. Dessemond, T. Kloidt, and M. C. Steil, in *Solid Fuel Cells IV*, M. Dokiya, O. Yamamoto, H. Tagawa, and S. C. Singhal, Editors, PV 95-1, p. 527, The Electrochemical Society Proceedings Series, Pennington, NJ (1995).
14. M. Kuznecov, P. Otschik, P. Obenaus, K. Eichler, and W. Schaffrath, *Russ. J. Electrochem.*, **40**, 1162 (2004).
15. B. C. H. Steele, *Solid State Ionics*, **75**, 157 (1995).
16. J. R. Smith, A. Chen, D. Gostovic, D. Hickey, D. Kundinger, K. L. Duncan, R. T. DeHoff, K. S. Jones, and E. D. Wachsman, *Solid State Ionics*, **180**, 90 (2009).
17. S. B. Adler, J. A. Lane, and B. C. H. Steele, *J. Electrochem. Soc.*, **143**, 3554 (1996).
18. M. Kleitz, L. Dessemond, H. Jimenez, F. Petitbon, R. Herbin, and E. Marchand, in *Proceedings of the 2nd European SOFC Forum*, U. Bossel and B. Thorstensen, Editors, European SOFC Forum, p. 443 (1996).
19. J. Mizusaki, K. Amano, S. Yamauchi, and K. Fueki, *Solid State Ionics*, **22**, 313 (1987).
20. N. Q. Minh, *J. Am. Ceram. Soc.*, **76**, 563 (1993).
21. A. Hammouche, E. Siebert, M. Kleitz, and A. Hammou, in *Proceedings of the First International Symposium on Solid Oxide Fuel Cells*, S. C. Singhal, Editor, PV 89-11, p. 265, The Electrochemical Society Proceeding Series, Pennington, NJ (1989).
22. L. G. J. de Haart, R. A. Kuipers, K. J. de Vries, and A. J. Burggraaf, *J. Electrochem. Soc.*, **138**, 1970 (1991).
23. D. Gostovic, J. R. Smith, D. P. Kundinger, K. S. Jones, and E. D. Wachsman, *Electrochem. Solid-State Lett.*, **10**, B214 (2007).
24. J. Sasaki, J. Mizusaki, S. Yamauchi, and K. Fueki, *Bull. Chem. Soc. Jpn.*, **54**, 1688 (1981).
25. A. D. Franklin, *J. Am. Ceram. Soc.*, **58**, 465 (1975).
26. A. Mitterdorfer and L. J. Gauckler, *Solid State Ionics*, **111**, 185 (1998).